

UC Santa Barbara

UC Santa Barbara Previously Published Works

Title

Enhanced Electrochemical Performance of Disordered Rocksalt Cathodes in a Localized High-Concentration Electrolyte

Permalink

<https://escholarship.org/uc/item/52z236vf>

Journal

Advanced Energy Materials, 14(27)

ISSN

1614-6832

Authors

Ahmed, Ridwan A

Koirala, Krishna P

Lee, Gi-Hyeok

et al.

Publication Date

2024-07-01

DOI

10.1002/aenm.202400722

Copyright Information

This work is made available under the terms of a Creative Commons Attribution License, available at <https://creativecommons.org/licenses/by/4.0/>

Peer reviewed

Enhanced Electrochemical Performance of Disordered Rocksalt Cathodes in a Localized High-Concentration Electrolyte

Ridwan A. Ahmed, Krishna P. Koirala, Gi-Hyeok Lee, Tianyu Li, Qian Zhao, Yanbao Fu, Lirong Zhong, Joseph D. Daddona, Mateusz Zuba, Carrie Siu, Ozgenur Kahvecioglu, Vincent S. Battaglia, Raphaële J. Clément, Wanli Yang,* Chongmin Wang,* and Wu Xu*

Lithium (Li)-rich transition metal oxide cathodes with a cation disordered rock salt structure (DRX) are increasingly gaining popularity for advanced Li batteries as they offer high capacity and cost benefits over the commonly used layered Li transition metal oxide cathodes. However, the performance of DRX cathodes and their applications are limited by severe side reactions between the cathode and the state-of-the-art carbonate-based electrolytes at high voltage of 4.8 V, transition metal dissolution, and structural instability of the cathode particles. In this work, an advanced localized high-concentration electrolyte (LHCE) is developed to form a stable cathode-electrolyte interphase and mitigate structural instability of the $\text{Li}_{1.13}\text{Mn}_{0.66}\text{Ti}_{0.21}\text{O}_2$ (LMTO) DRX during electrochemical cycling. Li||LMTO half cells with the LHCE demonstrate increased capacity, cycling stability, and superior rate capability compared with cells containing a conventional carbonate electrolyte. For instance, the Li||LMTO cells cycled in LHCE show a higher initial capacity of 205.2 mAh g^{-1} and a better capacity retention of 72.5% after 200 cycles at a current density of 20 mA g^{-1} than those with the conventional electrolyte (initial capacity of 187.7 mAh g^{-1} and capacity retention of 19.9%). This work paves the way to the development of practical DRX cathode-based high-energy Li batteries.


1. Introduction

There is a growing demand for lithium (Li)-ion batteries (LIBs) across various sectors and industries including communication, transportation, and grid storage. This poses stricter requirements such as high energy density, high power, materials sustainability, safety, and cost on this technology. Commercial LIBs typically utilize graphite anodes and layered Li transition metal oxides or phosphates cathodes, with limited specific capacity, safety issue and high cost.^[1,2] An innovative approach to realize high energy density batteries is to use anodes with high specific capacity and cathodes with high specific capacity and high operating voltage. Li metal is an ultimate anode material because of its ultrahigh theoretical specific capacity of 3860 mAh g^{-1} and the lowest redox potential of -3.040 V versus standard hydrogen electrode,^[3-6] but

R. A. Ahmed, L. Zhong, W. Xu
Energy and Environment Directorate
Pacific Northwest National Laboratory
Richland, WA 99354, USA
E-mail: wu.xu@pnnl.gov

K. P. Koirala
Physical and Computational Sciences Directorate
Pacific Northwest National Laboratory
Richland, WA 99354, USA

G.-H. Lee, W. Yang
Advanced Light Source
Lawrence Berkeley National Laboratory
Berkeley, CA 94720, USA
E-mail: wlyang@lbl.gov

 The ORCID identification number(s) for the author(s) of this article can be found under <https://doi.org/10.1002/aenm.202400722>

© 2024 The Authors. Advanced Energy Materials published by Wiley-VCH GmbH. This is an open access article under the terms of the [Creative Commons Attribution](#) License, which permits use, distribution and reproduction in any medium, provided the original work is properly cited.

DOI: 10.1002/aenm.202400722

T. Li, R. J. Clément
Materials Department and Materials Research Laboratory
University of California
Santa Barbara, CA 93106, USA

Q. Zhao, C. Wang
Environmental Molecular Sciences Laboratory
Pacific Northwest National Laboratory
Richland, WA 99354, USA
E-mail: chongmin.wang@pnnl.gov

Y. Fu, V. S. Battaglia
Energy Storage and Distributed Resources Division
Lawrence Berkeley National Laboratory
Berkeley, CA 94720, USA

J. D. Daddona
National Security Directorate
Pacific Northwest National Laboratory
Richland, WA 99354, USA

M. Zuba, C. Siu, O. Kahvecioglu
Applied Materials Division
Argonne National Laboratory
Lemont, IL 60439, USA

the challenges associated with Li metal anode such as high reactivity and dendrite growth have not been completely addressed for practical applications.^[7–9] On the cathode side, innovative cathode materials with high specific capacity/energy density surpassing those of state-of-the-art layered transition metal oxide cathodes are required for the realization of high energy density batteries. To this effect, Li-rich layered and disordered rock salt (DRX) transition metal oxide cathodes which allow for both transition metal redox and anionic oxygen (O) redox processes are gaining increased research interest.^[10–12] Among these, manganese (Mn)-based Li-rich DRX cathodes are particularly promising as they can deliver a specific capacity >300 mAh g⁻¹ and a specific energy above 1000 Wh kg⁻¹.^[13,14] In addition, Mn-based DRX cathodes are made up of low cost and earth abundant materials, and benefit from the thermal stability of Mn.^[15]

DRX cathodes exhibit a high specific capacity at a high cut-off voltage (≈ 4.8 V). However, the conventional LiPF₆/carbonate-based electrolytes commonly used in state-of-the-art LIBs become unstable and undergo oxidative decomposition when the cell voltage is above 4.3 V.^[16] In addition, the unstable cathode-electrolyte interphase (CEI) results in continued parasitic side reactions between cathode and electrolyte during electrochemical cycling.^[16–18] Additionally, the irreversible anionic redox process in DRX cathodes can release reactive O species, further promoting reactions with conventional carbonate-based electrolytes.^[19–21] These factors, along with the cathode particle cracking, transition metal reduction and dissolution are significant contributors to the observed capacity fading in DRX cathodes.^[19,22,23] Despite its importance, little effort has been directed toward the design of advanced electrolytes for DRX cathodes, some of which include the use of different additives in conventional electrolytes and the development of ionic liquid electrolytes.^[19,24] Meanwhile, most of these electrolytes still suffer from high voltage instability and decomposition, form an unstable and thick CEI, and promote structural instability of the DRX particles during electrochemical cycling.^[19] Recently, highly concentrated electrolytes (HCEs) have been utilized to enhance electrode reversibility of DRX cathodes.^[25–29] However, the practical application of HCEs in batteries faces limitations such as high viscosity, poor wettability, and high cost. To address these challenges, a potential solution involves forming a localized high-concentration electrolyte (LHCE) by the addition of a non-coordinating solvent or diluent to the HCE to combine the advantages of HCE with a relatively low viscosity, good wettability, and low cost.^[30] In addition, LHCEs have been shown to form an ultrathin, uniform, stable, and robust salt-derived CEI on nickel (Ni)-rich layered oxide cathodes with the charge cutoff voltage up to 4.4 V in full cells, which is due to the high concentration of anion-Li⁺-solvent aggregates.^[31–33] Despite the success of these LHCEs with relatively high voltage layered transition metal oxide cathodes,^[31,34,35] the performance of DRX cathodes cycled in this type of electrolyte has yet to be explored.

In this work, an LHCE based on a salt of Li bis(fluorosulfonyl)imide (LiFSI), a solvating solvent of dimethyl carbonate (DMC) with some ethylene carbonate (EC) as additive, and a diluent of 1,1,2,2-tetrafluoroethyl-2,2,3,3-tetrafluoropropyl ether (TTE) is developed for the high voltage Li_{1.13}Mn_{0.66}Ti_{0.21}O₂ (LMTO) DRX cathode. The synthesis and characterization of the LMTO active material can be found in the Supporting Informa-

tion for the supplementary experimental section, Figures S1 and S2, and Table S1 (Supporting Information). The performance of this LHCE in comparison with that of a conventional electrolyte of 1 M LiPF₆ in EC-DMC (1:2 by wt.) (abbreviated E-baseline) is evaluated in Li||LMTO half cells under 4.8 V. In addition, the chemical and structural evolution of the LMTO cathode, as well as the evolution of the interphase, are evaluated and characterized with electrochemical cycling in the two electrolyte systems of interest. The LHCE shows excellent compatibility with LMTO, forming a robust and stable CEI that effectively suppresses electrode/electrolyte side reactions and preserves the structural integrity of the LMTO particles. Consequently, Li||LMTO cells comprising the LHCE deliver an increased capacity and exhibit an improved cycling stability with outstanding charge and discharge rate capabilities.

2. Results and Discussion

2.1. Wettability and High Voltage Stability

The basic properties, including the ionic conductivity, the viscosity, the electrochemical stability window, and the wettability to the polyethylene (PE) separator, of both the conventional carbonate-based electrolyte and the LHCE were first evaluated, and the results are presented in Figures S3 and S4 (Supporting Information), respectively and summarized in Table 1. While the LHCE has a lower ionic conductivity and a higher viscosity than E-baseline (Figure S3a,b, Supporting Information), it has been demonstrated that the performance of Li batteries is not primarily governed by the electrolyte's conductivity and viscosity, but rather by the nature and properties of the electrode/electrolyte interphase as well.^[34] Linear sweep voltammetry (LSV) measurement indicates a high oxidative stability (≈ 5.0 V vs Li/Li⁺) for both the E-baseline and the LHCE employed in this study (Figure S3c, Supporting Information). This demonstrates the compatibility of both electrolytes with high voltage cathodes. However, the LHCE shows better wettability to the widely used PE separator with a lower contact angle of 28.9° compared to 41.2° for the E-baseline (Table 1; Figure S4, Supporting Information). It is also expected that the LHCE would enable the LMTO cathode to perform well because of its capability to form an advanced CEI.^[36,37]

2.2. Electrochemical Performance of Li||LMTO Cells

The electrochemical performance of the LHCE, by comparison with the E-baseline, was investigated in Li||LMTO half cells in a voltage range of 2.0–4.8 V at 30 °C. The long-term cycling stability of Li||LMTO cells was assessed at a current density of 20 mA g⁻¹ after 4 formation cycles at a current density of 10 mA g⁻¹. The evolution of the charge-discharge voltage profiles of Li||LMTO cells with E-baseline and LHCE is presented in Figure 1a. The cells with LHCE show a higher discharge capacity (226.5 mAh g⁻¹) at the first formation cycle under 10 mA g⁻¹ than the E-baseline cells, 211.1 mAh g⁻¹. In addition, the voltage profile evolution also reveals less voltage polarization for cells with LHCE than for cells with E-baseline (Figure 1a; Figure S5a, Supporting Information), indicating higher stability and reduced impedance build-up

Table 1. Basic properties of E-baseline and LHCE.

Electrolyte	Ionic conductivity at 25 °C [mS cm ⁻¹]	Viscosity at 25 °C [cP]	Oxidation voltage [V vs Li/Li ⁺]	Contact angle on PE [degree]
E-baseline	9.8	2.6	≈5.0	41.2
LHCE	2.4	5.0	≈5.0	28.9

in Li||LMTO cells with LHCE. Furthermore, the dQ/dV profiles of the cells with both electrolytes are similar during the 1st cycle (Figure S5b, Supporting Information). While there is no significant change in the intensity of the peaks in the dQ/dV profiles, there is a shift in the positions of the redox peaks at higher cycle numbers.

The long-term cycling stability results presented in Figure 1b and Figure S6 (Supporting Information) show that Li||LMTO cells with E-baseline deliver an initial capacity of 187.7 mAh g⁻¹ and a Coulombic efficiency (CE) of 92.7% at a current density of 20 mA g⁻¹. This is accompanied by a gradual capacity decay until about 160 cycles. After 160 cycles, the capacity decay becomes more severe resulting in a capacity of only 39.7 mAh g⁻¹ at the 200th cycle, which corresponds to a capacity retention of 19.9%. Moreover, there is a fast drop in the CE after ≈90 cycles, and it fluctuates after ≈170 cycles (Figure S6a, Supporting Information). The fast capacity decay and the drop in CE can be attributed to severe parasitic reactions of the E-baseline with both the Li an-

ode and the LMTO cathode, which will be elaborated on later. By comparison, Li||LMTO cells cycled in the LHCE show a higher capacity with an initial capacity of 205.2 mAh g⁻¹ and a CE of 94.7% at a current density of 20 mA g⁻¹. In addition, the LHCE enables the cells to exhibit a much-improved cycling stability delivering a capacity of 155.0 mAh g⁻¹ corresponding to a capacity retention of 72.2% after 200 cycles (Figure 1b). As opposed to the fluctuating CE of cells with E-baseline, the CE of cells with LHCE is stable with a value of 99.5% in the entire 200 cycles (Figure S6a, Supporting Information). Moreover, as shown in Figure S6b,c (Supporting Information), the initial specific energy and the energy retention after 200 cycles at 20 mA g⁻¹ of the Li||LMTO cells with LHCE are 665.2 Wh kg⁻¹ and 72.5%, much higher than with E-baseline (601.4 Wh kg⁻¹ and 19.9%, respectively).

The rate capabilities of the two electrolytes in Li||LMTO cells were investigated using both charge rate and discharge rate testing procedures. After three formation cycles at a current density of 10 mA g⁻¹, the charge rate capability was conducted using

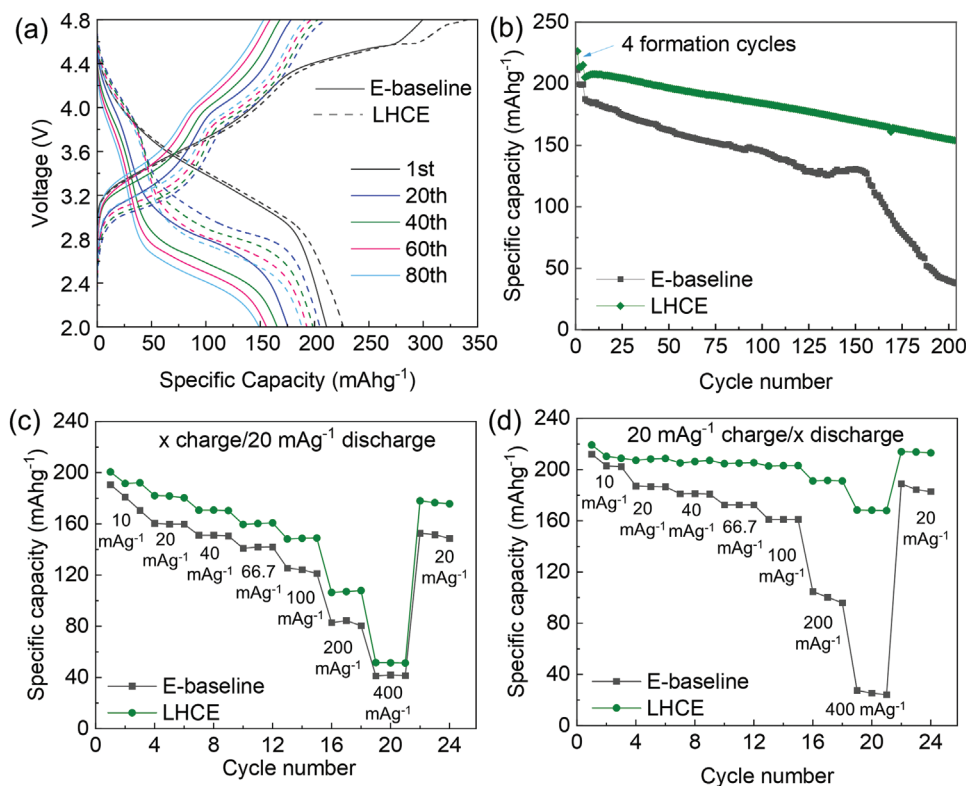


Figure 1. Electrochemical performances of Li||LMTO coin cells at 30 °C. a) Charge–discharge voltage profiles at selected cycles, b) long-term cycling stability at 20 mA g⁻¹ after four formation cycles at 10 mA g⁻¹, (c,d) rate capabilities under c) constant discharge current density of 20 mA g⁻¹ and varying charge current density (x mA g⁻¹) and d) constant charge current density of 20 mA g⁻¹ and varying discharge current density (x mA g⁻¹), where x = 10, 20, 40, 66.7, 100, 200, and 400 mA g⁻¹, respectively.

a constant discharge current density of 20 mA g⁻¹ and various charge current densities ranging from 10 to 400 mA g⁻¹. The same procedure was followed to determine the discharge rate capability, but with varying discharge current densities (ranging from 10 to 400 mA g⁻¹) and a constant charge current density of 20 mA g⁻¹. As shown in Figure 1c, cells with LHCE exhibit higher initial capacity and better charge rate capability than cells with E-baseline. In addition, cells with the LHCE show reduced voltage polarization at higher current densities compared to those with the E-baseline (Figure S7, Supporting Information). A similar trend is observed for the discharge rate capability shown in Figure 1d. The higher initial capacity delivered by the cells with LHCE can be linked to the better wettability of the LHCE to the PE separator as shown in Figure S4 (Supporting Information) compared with E-baseline, and the formation of ultrathin yet robust CEI on LMTO cathode and solid electrolyte interphase (SEI) on Li anode during the initial cycles, which will be elaborated upon later. Furthermore, the higher rate capability of Li||LMTO cells with LHCE is attributed to a fast electrode redox reaction facilitated by the formation of fast ion conductive CEI and SEI.

2.3. Structural Evolution of the LMTO Cathode in E-Baseline and LHCE

Structural transformation, irreversible O redox process, transition metal reduction and dissolution have been put forward to explain the rapid capacity fade observed for DRX-based cells.^[38–42] To examine these issues in the context of LMTO cycled in both E-baseline and LHCE, microstructural and chemical composition analyses were conducted on the pristine and cycled LMTO cathodes collected at the 100th discharged state. The assessment of surface compositions on LMTO was performed using energy-dispersive X-ray spectroscopy (EDS) in a scanning transmission electron microscope (STEM). Figure S8 (Supporting Information) illustrates the elemental distribution of LMTO active particle of the as-prepared electrode in the pristine state and the cycled states with E-baseline and LHCE. In the pristine cathode particle, a uniform distribution of Mn, titanium (Ti), and O is evident. Additionally, a distinct region of fluorine (F) clustering is observed in the pristine state, which could originate from the polyvinylidene fluoride (PVDF) binder material in the cathode composite. Since F is still present on the as-synthesized LMTO particle as shown in Figure S9 (Supporting Information), this suggests that the F is also likely from the residual LiF precursor used during the synthesis. The calcination of the LMTO sample with LiF precursor was aimed at achieving F doping of the LMTO; however, it was later confirmed that the F content in the as-synthesized LMTO was from little to none as revealed by the ¹⁹F solid-state NMR spectra in Figure S2 (Supporting Information). Upon cycling the cathode with E-baseline, a noticeable shift in the F distribution emerges, specifically a non-uniform thicker surface rich in F. The LMTO active cathode particles cycled in LHCE show a relatively thinner F-rich region in resemblance to the pristine particles.

The influence of electrolyte composition on the surface stability of the LMTO cathode and on the bulk transformations upon cycling was further assessed using high-angle annular dark-field (HAADF) and bright-field (BF) imaging in scanning

transmission electron microscopy (STEM) and selected area electron diffraction (SAED). The as-prepared LMTO cathode particles exhibit a surface devoid of cracks and porosity, as shown in Figure 2a. The electron diffraction patterns reveal a rock-salt type structure of cubic Fm-3m space group with short-range order. In a comparative study using STEM imaging in HAADF and BF modes of cathode particles collected after 100 cycles, it becomes apparent that the cathode's particle surface experienced significant damage in E-baseline, characterized by the formations of cracks and voids throughout the bulk of the particle, as shown in Figure 2b. In contrast, for the case of LHCE, the occurrence of cracks and voids on the cathode surface is markedly suppressed, as shown in Figure 2c. The resulting cathode particles exhibit a closer resemblance to the pristine particles, indicating an effective surface stabilization with LHCE. This implies that the mechanical integrity of LMTO cathode particles is well preserved when using the LHCE.

Additionally, we observed that both the LMTO cathode particles cycled in E-baseline and LHCE undergo a local phase transformation to a “delta phase” with spinel-like cation ordering, as has been observed in related systems.^[13,43,44] This result is confirmed by the electron diffraction patterns, which can be assigned to the cubic Fd-3m spinel space group. Increased polycrystallinity in the bulk of the cathode cycled with E-baseline, suggested by the elongated diffraction spots in the SAED pattern compared to the cathode cycled in LHCE, is also noted. Furthermore, we observed a thick amorphized CEI layer at the surface of cathode particles cycled in E-baseline compared to that in LHCE. It has been reported that such a thick and nonuniform surface layer increases the impedance of the cathode, thereby reducing the performance of cathodes.^[45] Overall, our observations indicate that LHCE results in more stable CEI, mitigating the surface degradation and reducing the bulk structural transformations during cycling, thus enhancing the stability of the LMTO cathode.

To gain further insight into the structural changes taking place in the LMTO cathode during cycling, ⁷Li solid-state nuclear magnetic resonance (NMR) spectroscopy was conducted on the pristine and the cycled LMTO electrodes stopped on discharge to 2.0 V after 100 cycles. As exhibited in Figure 3, the ⁷Li spectra exhibit two main resonances. The sharp signal centered ≈0 ppm is attributed to one or more Li-containing diamagnetic impurities, such as Li₂CO₃, LiF, or Li₂O/LiOH. The broad and highly shifted resonance, which is itself composed of many broad and overlapping signals, corresponds to a distribution of paramagnetic Li environments in the DRX structure, as has been discussed in more detail in the previous work.^[46–48] While the shape and intensity of the diamagnetic ⁷Li signal do not evolve significantly upon cycling, the average chemical shift and linewidth of the broad resonance associated with Li in DRX structure changes during cycling in both electrolyte systems, but much more significantly for the E-baseline. The ⁷Li signal observed for LMTO cycled with E-baseline is much reduced in intensity and significantly sharper than that observed for the pristine cathode, indicating a loss of Li inventory and a narrower distribution of Li chemical environments after cycling, consistent with local structural rearrangements and greater cation short-range ordering in the bulk cathode after cycling. On the other hand, the DRX ⁷Li signal for LMTO cycled with LHCE has a similar linewidth as that of the pristine cathode, but is reduced in intensity, which implies some

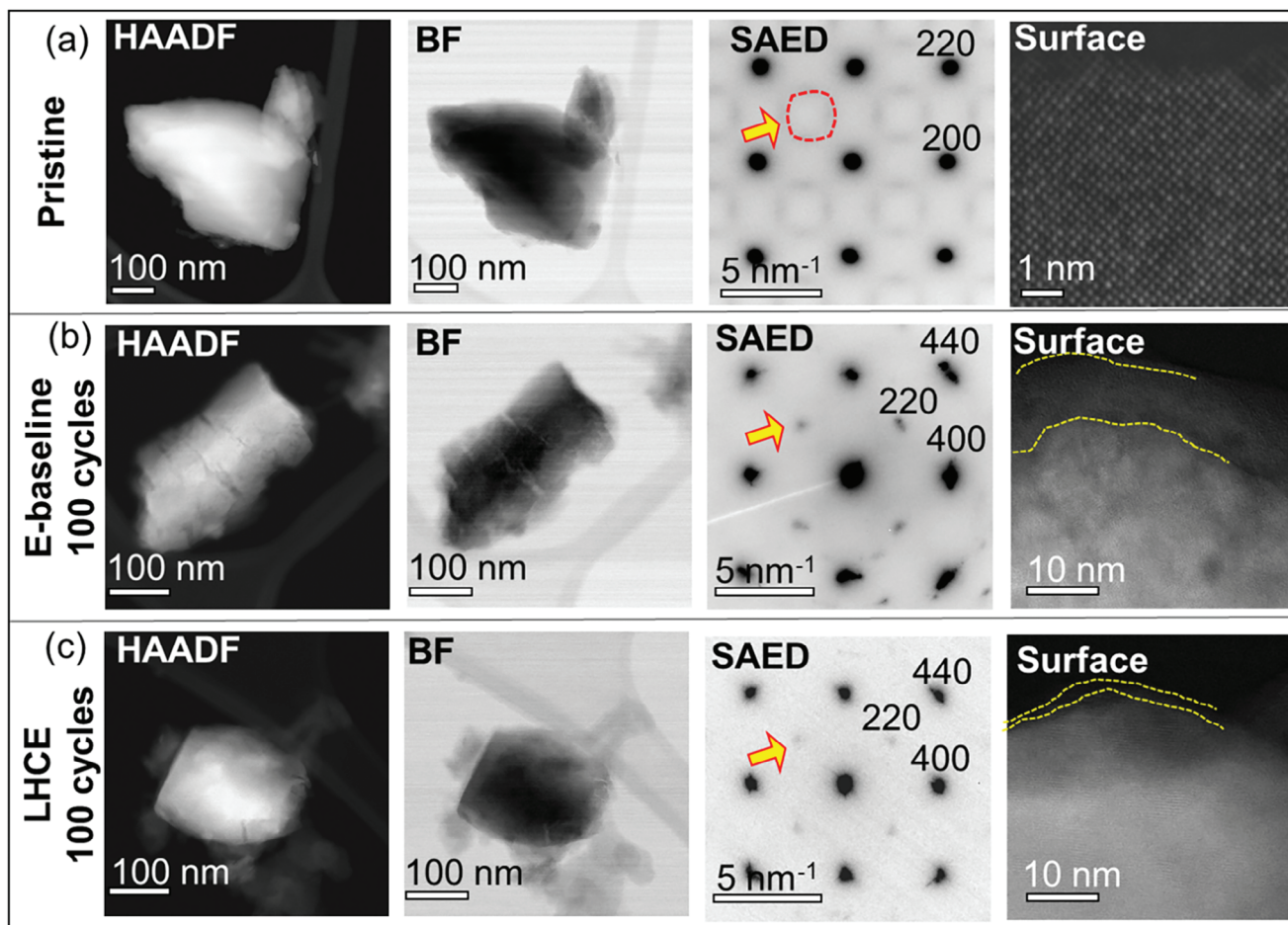


Figure 2. Comparison of surface and bulk structures of as-prepared LMTO cathode particles in pristine state and at 100th discharged state in E-baseline and LHCE. a) From left to right, HAADF and BF images show the representative particle at pristine state, the SAED pattern viewing along [001] zone axis confirms the cubic $Fm\bar{3}m$ space group with short range order (pointed by arrow), and the atomic resolution HAADF image shows the cubic lattice and crystalline surface viewing along [001] zone axis. b) From left to right, HAADF and BF images after 100 cycles in E-baseline show the porosity and crack in the particle, the SAED pattern confirms the cubic $Fd\bar{3}m$ spinel space group, and the particle surface (≈ 10 nm) is amorphous. c) From left to right, HAADF and BF images after 100 cycles in LHCE show the porosity and crack in the particle, the SAED pattern confirms the cubic $Fd\bar{3}m$ spinel space group, and the particle surface (≈ 1 nm) is amorphous.

loss of Li inventory but relatively minor bulk structure changes. Those results are in good agreement with the evolution of the microstructure of the LMTO particles as revealed by STEM, indicating reduced cracking, and pitting for the LMTO cathode cycled with the LHCE.

2.4. Postmortem Analyses of Li||LMTO Cells after 200 Cycles

The origin of the exceptional cycling performance of Li||LMTO cells with LHCE and the compatibility of the LMTO DRX with both E-baseline and LHCE were further investigated by performing microscopic and spectroscopic characterizations on both pristine and cycled LMTO electrodes harvested after 200 cycles. X-ray photoelectron spectroscopy (XPS) analysis was employed to examine the composition of the CEI on the LMTO electrode surface after 200 cycles. The results, presented in Figure 4a–c, show notable peaks related to the conductive carbon (C-C/C-H,

284.8 eV, C 1s) and the PVDF binder (C-F, ~ 290.7 eV and CF_2-CH_2 , ~ 287.5 eV, C 1s) on the surface of the pristine cathode. For F 1s spectra, the surface of the pristine LMTO electrode shows a strong C-F peak (~ 687.9 eV, F 1s) from PVDF and a strong LiF peak (~ 685.4 eV, F 1s). For the cycled LMTO electrodes, the C-F peak is significantly reduced especially for the one cycled in LHCE. This is possibly because the formed CEI after long cycling passivates the electrode surface allowing less C-F species to be detected. The LiF peak on the pristine electrode is associated with the LiF impurity on the as-prepared LMTO active material as observed in the STEM results (Figures S8 and S9, Supporting Information). As shown in Figure 4f about the atomic compositions of the elements detected on the electrode surfaces, the contents of C and F species in the CEI on LMTO cycled in LHCE are much lower than those in E-baseline, indicating less decomposition of the electrolyte components in the LHCE cells, which further implies the high quality of the CEI formed in the LHCE.

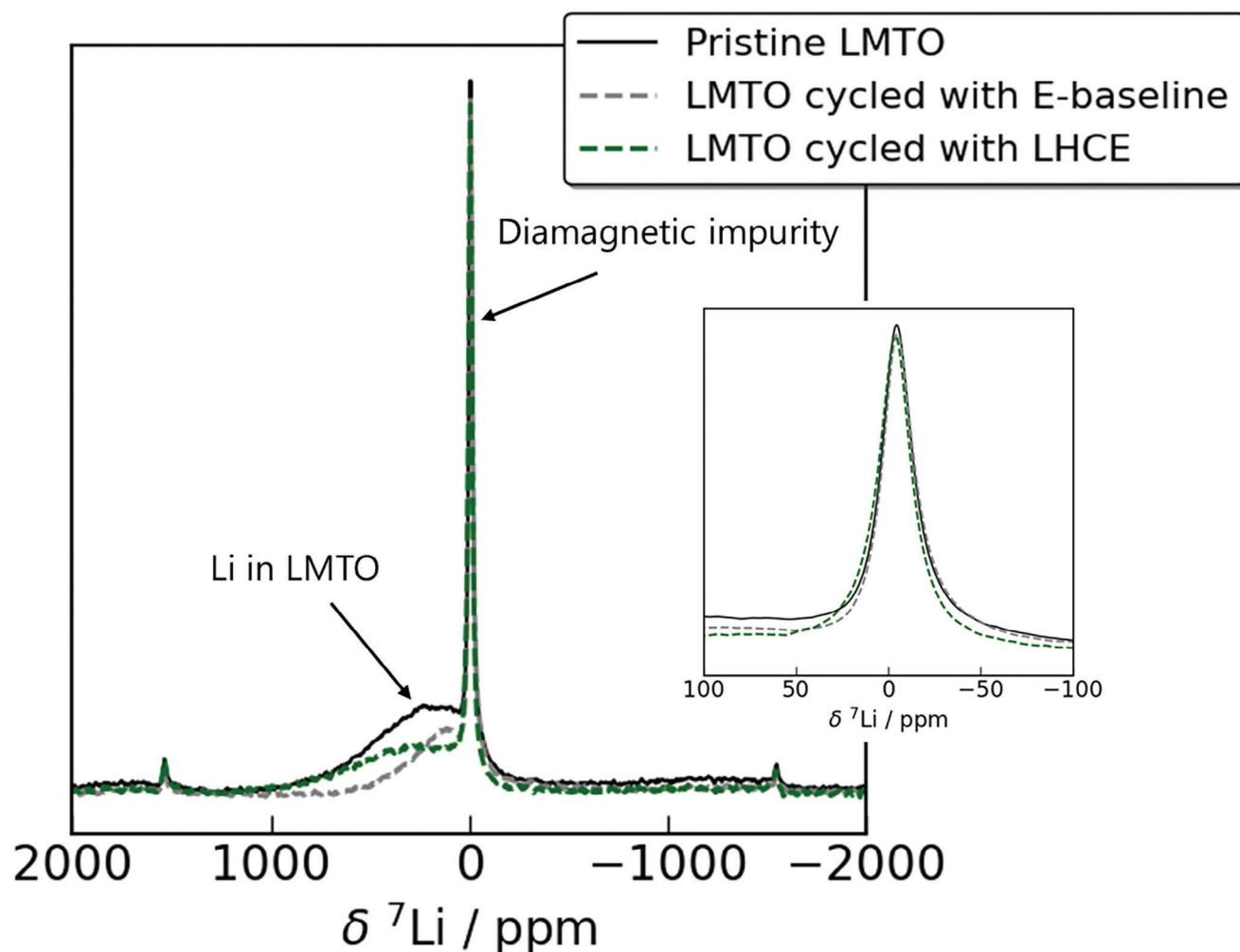


Figure 3. ^7Li spin echo solid-state NMR spectra of the pristine and cycled LMTO electrodes (100th discharge) in E-baseline and LHCE, which were collected at 100 MHz (2.35 T) and under 60 kHz magic angle spinning (MAS).

Additionally, for the S 2p spectra in Figure 4d, SO_x (~ 169.0 eV, S 2p) and S-N (~ 167.0 eV, S 2p) peaks are observed on the CEI with LHCE, suggesting decomposition of the LiFSI salt which has been previously reported to be beneficial to the mechanical strength and uniformity of the CEI layer, and improves cycling stability.^[31,34,37] The LMTO with E-baseline, on the other hand, shows the presence of LiPF_6 -derived species within the CEI, as evidenced by the Li_xPF_y (~ 136.0 eV, P 2p) and $\text{Li}_x\text{PO}_y\text{F}_z$ (~ 134.2 eV, P 2p) signals in Figure 4e. The decomposition of LiPF_6 salt anions and the high F atomic ratio (Figure 4f) suggest pronounced corrosion from the trace amount of HF in the E-baseline. This is detrimental to the structural integrity and the overall stability of the LMTO cathode and is again consistent with the STEM results discussed earlier.

In order to probe the surface CEI and the bulk redox chemistry upon electrochemical cycling, we further performed soft X-ray absorption spectroscopy (sXAS) and resonant inelastic X-ray scattering (RIXS) experiments at charged and discharged states of the LMTO electrodes cycled in E-baseline and LHCE, as shown in Figures 5 and 6.

O K-edge and C K-edge sXAS spectra were collected in the surface-sensitive total electron yield (TEY, Figure 5a,c) and the bulk sensitive total fluorescence yield (TFY, Figure 5b,d) modes with probe depths of ~ 10 and 150 nm, respectively.^[49] Other than the difference in the pre-edge feature of O-K spectra that stems from the different Mn states hybridized with O, which is discussed below, the most significant variation upon cycling could be seen from the $\text{C}=\text{O}$ π^* features ≈ 534 eV in both systems. The stronger intensity of this feature in TEY, compared with TFY spectra, indicates this comes from the surface carbonate species, instead of the bulk. Interestingly, the spectra collected from the LMTO samples cycled in LHCE display a more reversible surface carbonate cycling, which resembles the surface activities of some Li-rich layered compounds and deserves future studies.^[50]

The surface carbonate behavior indicated by the spectra here is consistent with the high voltage reaction in the dQ/dV profile (Figure S5b, Supporting Information), that is, because surface carbonate cycling takes place at only high voltages,^[50] the dQ/dV of LHCE system displays a sustained high voltage reaction for over a hundred cycles, but the E-baseline system shows the high-voltage reaction disappears within 50 cycles.

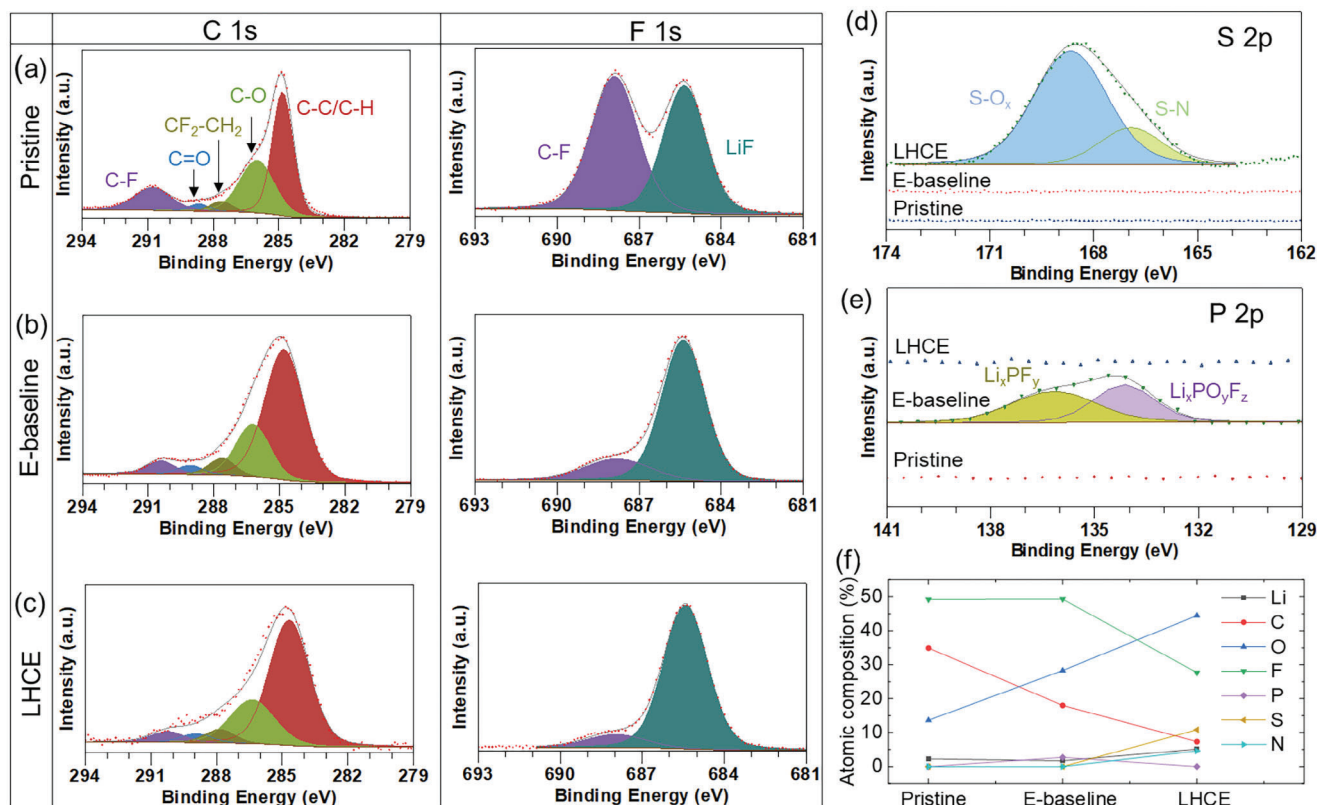


Figure 4. Comparison of the chemical compositions of the CEI on the pristine, cycled LMTO with E-baseline and LHCE collected at the 200th discharge state. XPS (C 1s and F 1s) spectra of a) pristine LMTO, b) LMTO cycled with E-baseline, c) LMTO cycled with LHCE, d) S 2p spectra of pristine and cycled LMTO with E-baseline and LHCE, e) P 2p spectra of pristine and cycled LMTO with E-baseline and LHCE, and f) atomic composition of elements on the surface of pristine and LMTO cycled with E-baseline and LHCE.

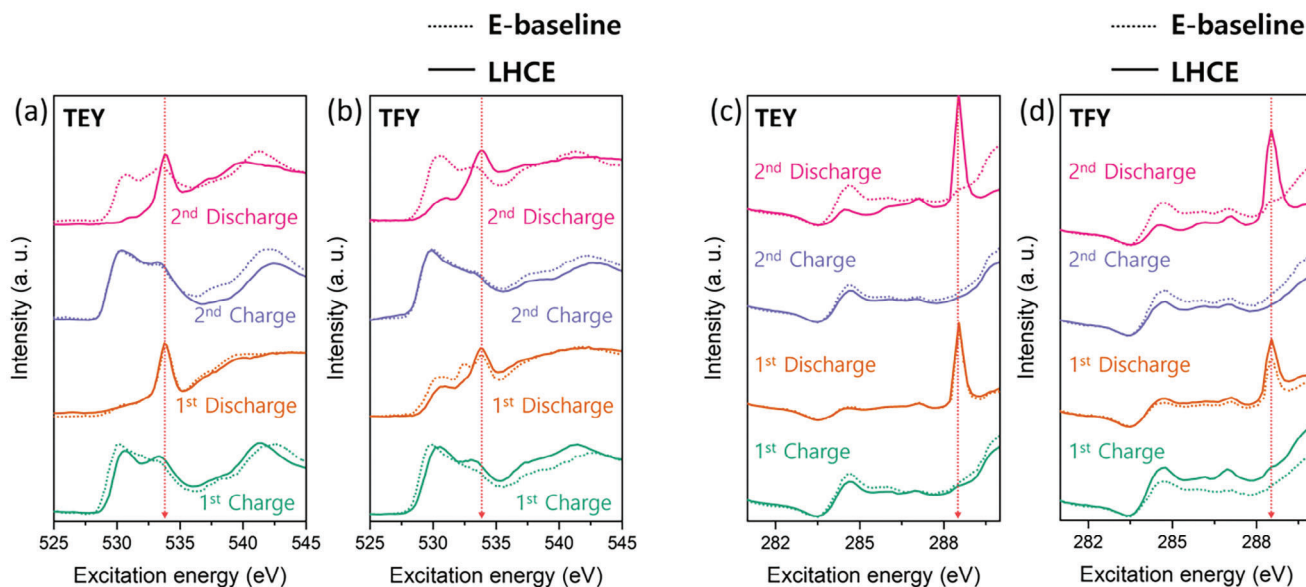


Figure 5. Soft X-ray absorption spectroscopy (sXAS) results of cycled cathodes in E-baseline (dotted lines) and LHCE (solid lines) for O (a,b) & C (c,d) K-edge, collected through TEY (a,c) and TFY (b,d) mode. The red dashed lines indicate the signatures of carbonate species.^[50]

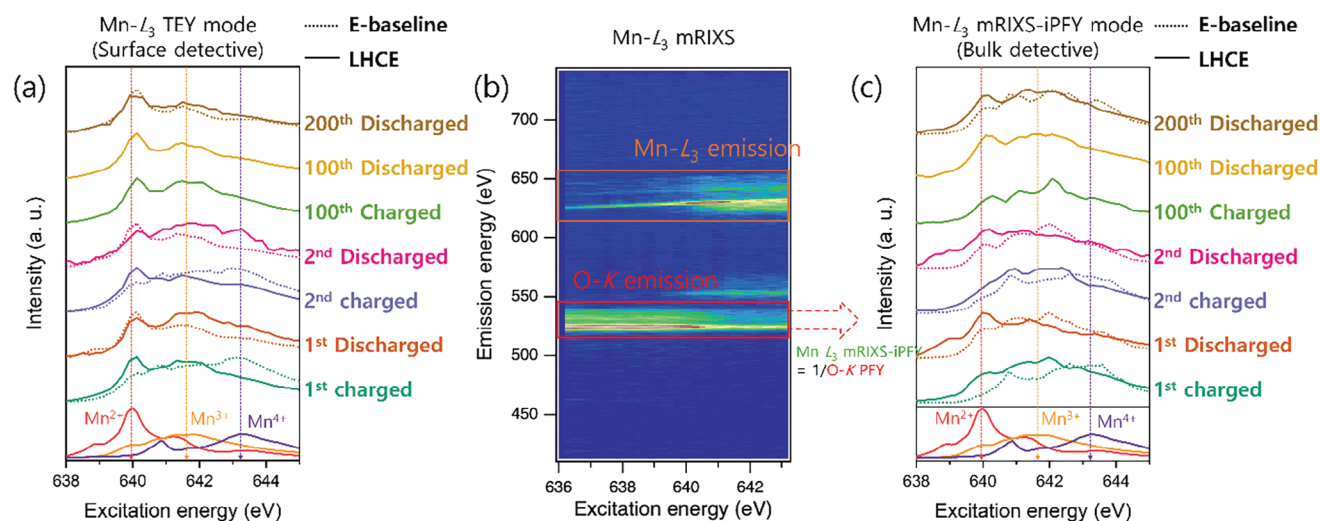


Figure 6. Soft X-ray spectroscopy Mn L_3 -edge results of cycled cathodes in E-baseline (dotted lines) and LHCE (solid lines). The Mn- L_3 sXAS spectra are collected by a) TEY mode and c) mRIXS-iPFY mode. The mRIXS map in Figure 6b is just one example obtained from 1st charged state of E-baseline sample, and the area where iPFY signals are extracted is indicated by the red rectangle. All iPFY spectra in (c) are extracted in the same way from mRIXS maps collected from each sample. The red, orange, and purple dashed lines indicate the major peak positions of reference $Mn^{2+/3+/4+}$ spectra of MnO , Mn_2O_3 , and Li_2MnO_3 , respectively.

Mn-L spectra correspond to direct excitations to the Mn-3d states, providing a sensitive probe of the Mn oxidation states.^[51,52] The surface sensitive TEY spectra shown in Figure 6a display a clear contrast between the two LMTO electrodes cycled in the two electrolyte systems: The surface low-valence Mn^{2+} feature ≈ 640 eV, which is typical for CEI, remains fairly stable upon cycling of the electrodes in LHCE; however, the E-baseline resulted samples show dramatic variation between charge and discharge states, indicating a much more stable CEI on the electrode surfaces generated by LHCE.

Figure 6b shows a typical Mn-L RIXS map that offers bulk-sensitive inverse partial fluorescence yield (iPFY) signal channels, which provides the non-distorted fluorescence channel for extracting bulk-sensitive L-edge signals.^[49] It is intriguing to see that, although both systems display line shape variation of the bulk-sensitive RIXS-iPFY spectra, an enhanced $Mn^{2+/3+/4+}$ redox behavior in LHCE, indicated by the variation of the Mn^{2+} peak ≈ 640 eV (Figure 6c) that is stronger than that in E-baseline sample. Such a line shape variation is sustained in the 100th cycle charge/discharge states, and at 200th cycle, the Mn^{2+} feature of LHCE remains stronger than the E-baseline sample at discharged state. The spectroscopic findings indicate that the LHCE optimizes the CEI formation and enhances the bulk Mn redox activities.

In more general term, it is widely recognized that the various bulk structural features, such as short-range-order,^[53] Jahn–Teller distortion of Mn^{3+} and partial spinel formation,^[13] affect the electrochemical properties of DRX. However, the coupling between surface and bulk through mass transport could indeed induce surface controlled bulk processes, such as cation dissolution and O loss, directly affecting the bulk structure. The present case involving electrolyte modification for DRX to optimize the formation of CEI layer, along with other surface modification techniques,^[54,55] directly demonstrate that controlling the surface process is essential

for stabilizing bulk lattice structure toward stable cycling of DRX.

We also investigated the morphology of the cycled Li metal anodes after 200 cycles and the composition of the SEIs using SEM and XPS analyses, and the results are presented in Figure 7. The SEM images shown in Figure 7a,b reveal a more severe corrosion in the Li metal anode with the E-baseline than with the LHCE. Furthermore, the XPS spectra in Figure 7c show that the E-baseline derived SEI has a stronger C=O (288.5 eV, C 1s) signal. Additionally, the F 1s spectra is dominated by the $Li_xPO_yF_z$ (≈ 686 eV) resulting from the decomposition of the $LiPF_6$ salt in the E-baseline. In contrast, the LHCE derived SEI is dominated by a diluent derived C-F (687.9 eV, F 1s) signal and LiF (≈ 685 eV, F 1s) signal (Figure 7d). The constituents of the SEI in the LHCE effectively suppress solvent decomposition during charge/discharge cycles and hence improve the stability of the Li metal anode. The obtained results show that not only is LHCE able to effectively passivate the LMTO cathode and reduce the cathode structural degradation but also able to form a stable and robust SEI layer on the Li metal anode as compared with E-baseline which forms a thick and weak SEI layer on the Li surface. Thus, the formation of stable and robust SEI on the Li metal surface by the LHCE also contributes to the improved electrochemical performance observed for the Li||LMTO cells with LHCE.

3. Discussion

According to the design principle of LHCEs and the previous characterization results on electrolyte structures of LHCEs and conventional electrolytes,^[30,31] the solvation structure of Li^+ ions in LHCEs comprises a very small amount of free solvent molecules and a large fraction of anions, forming contact ion pairs (CIPs) and aggregates (AGGs), while the conventional electrolytes have plenty of free solvent molecules and solvent-separated ion pairs (SSIPs).^[30,31,56]

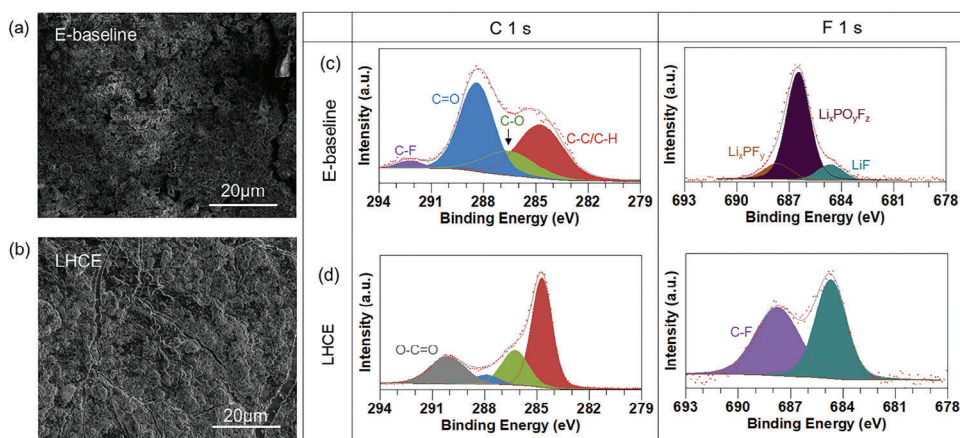


Figure 7. Comparison of the surface morphologies and chemical compositions of the SEIs of cycled Li metal anodes with E-baseline and LHCE collected at the 200th discharge state. SEM images of the surface of the Li metal cycled in a) E-baseline and b) LHCE. XPS (C 1s and F 1s) spectra of Li metal cycled with c) E-baseline and d) LHCE.

Such differences in Li^+ solvation structures in the two types of electrolytes explain the very different electrolyte reduction and oxidation reactions taking place at the anode and cathode during charge and discharge processes, respectively, resulting in differences in the SEI formed at the surface of the anode and the CEI formed at the surface of the cathode, respectively. Anion- Li^+ -solvent CIPs and AGGs in LHCEs are reduced or oxidized to form an SEI or a CEI that is rich in salt-derived species (dominated by inorganic components), such as LiF and other compounds depending on the nature of the anion.^[30,31] In contrast, Li^+ -solvent SSIPs in conventional electrolytes decompose to generate an SEI or a CEI that is dominated by organic species. In a recent report by Xu et al.,^[57] an SEI rich in organic species showed a higher electronic conductivity than the one enriched with inorganic species, allowing more and continuous decomposition of electrolyte components to yield thick and ionic resistant SEI. In contrast, an SEI dominated by inorganic species lowers the electronic conductivity, preventing further decomposition of the electrolyte and yielding a thinner and more ionically conductive SEI. A similar behavior is expected for the CEI formed at the cathode surface. Therefore, in this work, as demonstrated from the characterization results by STEM, EDS, solid-state NMR, sXAS and XPS, the LHCE leads to the formation of a thin but robust CEI that is rich in inorganic species on the LMTO surface, passivating the LMTO cathode to prevent a continued reaction between the LMTO cathode and the electrolyte, and consequently leading to the lattice structural stability of LMTO cathode upon cycling as evidenced by the very limited changes in surface and bulk structures of the LMTO particles. On the contrary, for the case of the baseline electrolyte, the CEI on the LMTO surface is rich in organic species with a high propensity of electron leakage, which correspondingly leads to a continued reaction between the LMTO cathode and the electrolyte upon battery cycling as evidenced by the thick CEI and severe lattice structural degradation in LMTO, featuring intragranular cracking and void formation. It has been well demonstrated that, for the case of Li-rich cathodes, void formation is closely related to lattice O loss.^[54,55,58] Lattice doping of F in DRX has been demonstrated to be an effective

way for stabilizing the surface O.^[54,55] Yet, it is not clear how F doping affects CEI layer formation. The presently observed markedly differences on the lattice structural stability of LMTO when cycled in different electrolytes clearly reveal the critical role of a passivating CEI layer for preventing the O loss from the Li-rich cathode. It is demonstrated that proper design of electrolyte can lead to the formation of passivating CEI on DRX or other cathode materials, alleviating cathode surface and bulk structure evolution upon battery cycling, and correspondingly maintaining the designed properties of the cathode material toward optimized electrochemical performance of high energy density batteries.

4. Conclusion

An advanced LHCE is developed for a high voltage and high energy density Li-rich and Mn-rich DRX cathode LMTO. The developed LHCE shows a high oxidation voltage of ≈ 5 V versus Li/Li⁺ and a good wettability on the commercial PE separator. The performance of the LHCE in comparison to the conventional electrolyte (E-baseline) is demonstrated in Li||LMTO cells. The results obtained show that an increased initial capacity (205.2 mAh g^{-1}), cycling stability with a capacity retention of 72.5% after 200 cycles at 20 mA g^{-1} and excellent charge/discharge rate capabilities (up to 100 and 400 mA g^{-1} , respectively) can be achieved when LHCE is used in Li||LMTO cells instead of the conventional carbonate-based electrolyte where only 187.7 mAh g^{-1} of initial capacity and 19.9% of capacity retention can be obtained. To elucidate the origin of the exceptional performance with LHCE, both surface and bulk structural characterizations were conducted on both pristine and cycled LMTO cathodes. Both STEM and solid-state NMR results show that a stable CEI is formed on the LMTO with the LHCE, mitigating both surface degradation and reducing bulk structural transformation during cycling. This is further corroborated by the XPS results, which show the presence of salt-derived species in the CEI and SEI layers that have previously been reported to be beneficial to the mechanical strength and uniformity of interphase layers. Additionally, the sXAS results confirm that LHCE not only modifies the CEI formation but also the

bulk redox activities. The results obtained in this work demonstrate that developing an advanced electrolyte such as LHCE for Mn-rich DRX cathodes will alleviate most of the issues associated with these cathode materials and thus facilitate the practical applications of DRX cathodes in high energy density batteries.

5. Experimental Section

Electrolyte and Electrode Preparation: The baseline electrolyte of 1 M LiPF₆ in EC-DMC (1:2 by wt.) and the LHCE of LiFSI-2DMC-0.2EC-3TTE (by mol.) were prepared by dissolving LiPF₆ salt in EC-DMC mixture or LiFSI salt in DMC-EC-TTE mixture, respectively in the designed weight or molar ratio. This was carried out in a purified Ar-filled MBraun glovebox, with oxygen and moisture content <1 ppm. The LMTO electrode laminates were fabricated in the Lawrence Berkeley National Laboratory (LBNL) facility with 75 wt.% carbon-coated LMTO powder as active material, 10 wt.% Denka black (DB), 5 wt.% carbon nanotube (CNT) and 10 wt.% PVDF. The LMTO electrode laminates had a mass loading of LMTO of 4.8 mg cm⁻² and were punched into half inch diameter disks and dried under vacuum at a temperature of 130 °C for at least 12 h before use. Li metal chips having thickness of 250 μm and diameter of 1.55 cm were purchased from MTI Corporation USA and used as received.

Electrochemical Tests: Electrolyte conductivities were measured between -40 and 60 °C using a Bio-Logic MCS 10 fully integrated multi-channel conductivity spectroscopy. The electrochemical stability window of each electrolyte was evaluated by linear sweep voltammetry (LSV) measurements using Bio-Logic SAS (VMP-300) with Li as both the reference electrode and the counter electrode and LiMn₂O₄ (LMO) electrode as the working electrode.

Each of the Li||LMTO coin cells was assembled with a piece of LMTO cathode, a piece of PE separator, a 250 μm thick Li metal anode, and 75 μL of electrolyte. An aluminum (Al)-clad positive case with an extra Al foil (19.0 mm diameter) inserted between the positive case and the LMTO cathode disk was used during the cell assembly. This was to prevent anodic corrosion of the stainless-steel positive case in electrolytes at high voltages. For the electrochemical cycling stability test the cells first underwent four formation cycles at a current density of 10 mA g⁻¹, then were cycled at 20 mA g⁻¹. However, for the charge rate capability test, the cells were first subjected to 3 formation cycles at a current density of 10 mA g⁻¹, then cycled at a constant discharge current density of 20 mA g⁻¹ and various charge current densities ranging from 20 to 400 mA g⁻¹. The same procedure was followed for the discharge rate capability, but with varying discharge current densities from 20 to 400 mA g⁻¹ and a constant charge current density of 20 mA g⁻¹. The cutoff voltage range was 2.0–4.8 V and the testing temperature was 30 °C.

Transmission Electron Microscopy (TEM): For transmission electron microscopic imaging, the pristine and cycled particles were dispersed onto TEM lacey carbon grids in an Ar-filled glovebox. Electron diffraction images were conducted on a Titan 80–300TM scanning/transmission electron microscope operated at 300 kV. HAADF/BM imaging and EDS data were collected using a Spectra Ultra S/TEM with a new generation Ultra-X EDS detector at an acceleration voltage of 300 kV. To avoid major beam damage on the samples, the imaging and EDS data were acquired with the Ultra-X instrument at a probe current of 30 pA.

Soft X-Ray Absorption Spectroscopy (sXAS): C, O K-edges, and Mn L₃-edge sXAS spectra were collected at beamline 8.0.1 in Advanced Light Source, LBNL. The samples charged at various states and cycles were transferred to the glovebox for sampling and pasted on the Cu tape for the measurement. An airtight transfer kit was used to transfer the sample from the glovebox to the measurement chamber. For the C and O K-edge sXAS spectra collection, total fluorescence yield (TFY; detecting <200 nm from the surface) and total electron yield (TEY; detecting <10 nm from the surface) modes were used. For Mn L₃-edge, TEY mode and map of resonant inelastic X-ray scattering-inverse partial fluorescence yield (mRIXS-iPFY) mode was used.

Map of resonant inelastic X-ray scattering-inverse partial fluorescence yield (mRIXS-iPFY) Mn-L₃ mRIXS-iPFY was extracted through the formula

iPFY = a/PFY_O, where a is a normalization coefficient, PFY_O is extracted by integrating the fluorescence intensity within the O-K emission energy range (490 to 530 eV) on the Mn-L₃ mRIXS. Mn-L₃ mRIXS-iPFY was used in this work instead of TFY to avoid the distortion observed in the conventional TFY caused by emission signals from oxygen.

Solid-State Nuclear Magnetic Resonance (NMR) Spectroscopy: ⁷Li solid-state NMR spectra of the pristine and cycled LMTO cathodes when cycled with E-baseline and LHCE electrolytes were acquired using solid-state NMR spectra were acquired using a wide bore Bruker BioSpin spectrometer equipped with a DMX 500 MHz console and a custom-made 1.3 mm, single channel broadband magic angle spinning (MAS) probe tuned to ⁷Li (38.9 MHz). The measurement was operated at a low magnetic field of 2.35 T (100 MHz for ¹H) to reduce paramagnetic broadening. ⁷Li NMR spectra were obtained using a rotor synchronized spin-echo sequence (90° – t_R – 180° – t_R) with 90° radio frequency (RF) pulses of 0.45 μs. ⁷Li chemical shifts were externally referenced against a 1 M aqueous LiCl solution (δ_{iso} = 0 ppm). A recycle delay of 20 s was used throughout, sufficiently long for all paramagnetic ⁷Li spins within the DRX structure to re-equilibrate between scans. To prepare the materials for characterization, the cathode current collectors were first obtained through disassembling the cycled cells. Then the active cathode materials were scratched from the current collector and loaded into the NMR rotors. All battery disassembly and sample loading steps were conducted in Ar-filled glovebox. The rotors with samples were spun at 60 kHz MAS using dry nitrogen. The NMR data was processed using the Bruker TopSpin 3.6.0 software.

X-Ray Photoelectron Spectroscopy (XPS): XPS analysis was performed on a Physical Electronics Quantera Scanning X-ray Microprobe (Physical Electronics, Germany). The system uses a focused monochromatic Al Kα (1486.7 eV) source for excitation. The survey scans were collected for quantifying the atomic composition of elements on the surface, using a pass-energy of 140 eV with a step size of 0.5 eV. High-energy resolution C1s, O1s, F1s, S2p, and P2p spectra were collected using a pass-energy of 69 eV with a step size of 0.125 eV. The obtained spectra were fitted with the CasaXPS software with the binding energy was calibrated with C 1s at 284.8 eV.

Viscosity Measurement: The viscosity of the electrolytes as a function of temperature was measured using an Anton Paar rheometer (MCR-101; Ashland, VA, USA). Double gap measuring system DG26.7 SS coupled with a C-PTD200 cell was used. A Peltier system built in the rheometer was employed for temperature control. A temperature ramp was applied to the electrolyte samples during measurements. The temperature was set at 0 °C to start the measurements. Once a measurement was started, temperature was increased linearly with time from 0 to 60 °C in a duration of 45 min while the viscosity was measured and recorded with the values logged in every 30 sec. A constant shear rate of 50 1/s was used for all measurements. After each sample measurement, the DG26.7 measuring system was disassembled for washing and drying, and then reassembled for a new sample. A nitrogen flow through the measuring system was established to minimize the sample exposure to air.

Contact Angle Measurement: The contact angle of the electrolyte on PE separator was measured using a ramé-hart Model 590 goniometer with DROPimage Advanced software. A 10-μL drop of electrolyte was applied to the PE separator for each trial using an automated dispensing system included in the instrument, and the contact angle of the drop resting on the substrate was measured every 0.05 s for 0.5 s. For trials where the electrolyte was absorbed by the substrate, the contact angle at the moment of contact between the electrolyte and substrate was measured.

Supporting Information

Supporting Information is available from the Wiley Online Library or from the author.

Acknowledgements

R.A.A., K.P.K., and G.-H.L. contributed equally to this work. This work was funded by the Assistant Secretary for Energy Efficiency and

Renewable Energy, Vehicle Technologies Office of the U.S. Department of Energy (DOE) through the DRX+ Consortium under the contract no. DE-AC05-76RL01830 for Pacific Northwest National Laboratory (PNNL) and DE-AC02-05CH11231 for Lawrence Berkeley National Laboratory (LBNL). Part of the microscopic and spectroscopic characterizations were performed in the William R. Wiley Environmental Molecular Sciences Laboratory (EMSL), a national scientific user facility sponsored by DOE's Office of Biological and Environmental Research and located at PNNL. Part of the electron microscopy work is carried out by using instruments that are funded in part by a grant from the Washington State Department of Commerce's Clean Energy Fund. PNNL is operated by Battelle for the DOE under Contract DE-AC05-76RL01830. This work made use of the shared MRL Spectroscopy facility of the UC Santa Barbara MRSEC (DMR 2308708), a member of the Materials Research Facilities Network (<http://www.mrfn.org>). Baseline LMTO cathode material synthesis reported in this paper was performed at the Materials Engineering Research Facility (MERF), Argonne National Laboratory (ANL). The MERF was supported by the DOE, Office of Energy Efficiency and Renewable Energy, and the Vehicle Technologies Office. The salt LiFSI was provided by Dr. Kazuhiko Murata of Nippon Shokubai Co., Ltd. Soft X-ray experiments were performed at BL 8.0.1 of the Advanced Light Source (ALS), a DOE Office of Science User Facility, under contract no. DE-AC02-05CH11231.

Conflict of Interest

The authors declare no conflict of interest.

Data Availability Statement

The data that support the findings of this study are available from the corresponding author upon reasonable request.

Keywords

cathode-electrolyte interphase, disordered rock salt cathode, electrolyte, lithium metal, structural integrity

Received: February 20, 2024
Revised: April 10, 2024
Published online: May 14, 2024

- [1] L. Azhari, B. Sousa, R. Ahmed, R. Wang, Z. Yang, G. Gao, Y. Han, Y. Wang, *ACS Appl Mater Interfaces* **2022**, *14*, 46523.
- [2] J. B. Goodenough, *J. Am. Chem. Soc.* **2013**, *4*, 1167
- [3] J. G. Zhang, W. Xu, J. Xiao, X. Cao, J. Liu, *Chem. Rev.* **2020**, *120*, 13312.
- [4] P. Albertus, S. Babinec, S. Litzelman, A. Newman, *Nature Energy* **2017**, *3*, 16.
- [5] D. Lin, Y. Liu, Y. Cui, *Nat. Nanotechnol.* **2017**, *12*, 194.
- [6] W. Xu, J. Wang, F. Ding, X. Chen, E. Nasybulin, Y. Zhang, J.-G. Zhang, *Energy Environ. Sci.* **2014**, *7*, 513.
- [7] B. Acebedo, M. C. Morant-Miñana, E. Gonzalo, I. Ruiz de Larramendi, A. Villaverde, J. Rikarte, L. Fallarino, *Adv. Energy Mater.* **2023**, *13*, 2203744.
- [8] R. A. Ahmed, N. Ebechidi, I. Reisy, K. Orisekeh, A. Huda, A. Bello, O. K. Oyewole, W. O. Soboyejo, *J. Power Sources* **2022**, *521*, 230939.
- [9] Q. Wang, B. Liu, Y. Shen, J. Wu, Z. Zhao, C. Zhong, W. Hu, *Adv. Sci.* **2021**, *8*, 2101111.
- [10] D. Chen, J. Ahn, G. Chen, *ACS Energy Lett* **2021**, *6*, 1358.
- [11] R. J. Clément, Z. Lun, G. Ceder, *Energy Environ. Sci.* **2020**, *13*, 345.
- [12] P. Rozier, J. M. Tarascon, *J. Electrochem. Soc.* **2015**, *162*, A2490.

- [13] Z. Cai, B. Ouyang, H.-M. Hau, T. Chen, R. Giovine, K. P. Koirala, L. Li, H. Ji, Y. Ha, Y. Sun, J. Huang, Y. Chen, V. Wu, W. Yang, C. Wang, R. J. Clément, Z. Lun, G. Ceder, *Nat. Energy* **2023**, *9*, 27.
- [14] H. Zhang, X. Gao, Q. Cai, X. Zhang, Y. Tian, M. Jia, W. Xie, Y. Du, X. Yan, *J. Mat. Chem.* **2023**, *11*, 8426.
- [15] M. M. Thackeray, J. R. Croy, E. Lee, A. Gutierrez, M. He, J. S. Park, B. T. Yonemoto, B. R. Long, J. D. Blauwkamp, C. S. Johnson, Y. Shin, W. I. F. David, *J. Sustainable Energy & Fuels* **2018**, *2*, 1375.
- [16] J. Kasnatscheew, M. Evertz, B. Streipert, R. Wagner, R. Klöpsch, B. Vortmann, H. Hahn, S. Nowak, M. Amereller, A. C. Gentschev, P. Lamp, M. Winter, *Phys. Chem. Chem. Phys.* **2016**, *18*, 3956.
- [17] W. Cai, Y. Deng, Z. Deng, Y. Jia, Z. Li, X. Zhang, C. Xu, X. Q. Zhang, Y. Zhang, Q. Zhang, *Adv. Energy Mater.* **2023**, *13*, 01396.
- [18] M. Evertz, F. Horsthemke, J. Kasnatscheew, M. Börner, M. Winter, S. Nowak, *J. Power Sources* **2016**, *329*, 364.
- [19] H. Chung, Z. Lebens-Higgins, B. Sayahpour, C. Mejia, A. Grenier, G. E. Kamm, Y. Li, R. Huang, L. F. J. Piper, K. W. Chapman, J.-M. Doux, Y. S. Meng, *J. Mater. Chem. A* **2021**, *9*, 1720.
- [20] Q. Li, Y. Wang, X. Wang, X. Sun, J. N. Zhang, X. Yu, H. Li, *ACS Appl. Mater. Interfaces* **2020**, *12*, 2319.
- [21] K. Zhou, C. Zhang, Y. Li, X. Liu, J. Liu, Z. Lun, Y. Yang, *Chemical Engineering Journal* **2023**, *464*, 142709.
- [22] M. Luo, S. Zheng, J. Wu, K. Zhou, W. Zuo, M. Feng, H. He, R. Liu, J. Zhu, G. Zhao, S. Chen, W. Yang, Z. Peng, Q. Wu, Y. Yang, *J. Mater. Chem. A* **2020**, *8*, 5115.
- [23] D. Chen, W. H. Kan, G. Chen, *Adv. Energy Mater.* **2019**, *9*, 01255.
- [24] J.-P. Brinkmann, N. Ehteshami-Flammer, M. Luo, M. Leißing, S. Röser, S. Nowak, Y. Yang, M. Winter, J. Li, *ACS Applied Energy Mater* **2021**, *4*, 10909.
- [25] A. Kanno, Y. Ugata, I. Ikeuchi, M. Hibino, K. Nakura, Y. Miyaoka, I. Kawamura, D. Shibata, T. Ohta, N. Yabuuchi, *ACS Energy Lett* **2023**, *8*, 2753.
- [26] N. Shimada, Y. Ugata, S. Nishikawa, D. Shibata, T. Ohta, N. Yabuuchi, *Energy Advances* **2023**, *2*, 508.
- [27] N. Takeda, I. Ikeuchi, R. Natsui, K. Nakura, N. Yabuuchi, *ACS Applied Energy Mater* **2019**, *2*, 1629.
- [28] M. A. Cambaz, B. P. Vinayan, H. Euchner, S. A. Pervez, H. Gesswein, T. Braun, A. Gross, M. Fichtner, *ACS Appl. Mater. Interfaces* **2019**, *11*, 39848.
- [29] M. A. Cambaz, B. P. Vinayan, S. A. Pervez, R. E. Johnsen, H. Geßwein, A. A. Guda, Y. V. Rusalev, M. K. Kinyanjui, U. Kaiser, M. Fichtner, *Chem. Mater.* **2019**, *31*, 7941.
- [30] X. Cao, H. Jia, W. Xu, J.-G. Zhang, *J. Electrochem. Soc.* **2021**, *168*, 010522.
- [31] D. J. Kautz, X. Cao, P. Gao, B. E. Matthews, Y. Xu, K. S. Han, F. Omenya, M. H. Engelhard, H. Jia, C. Wang, J. G. Zhang, W. Xu, *Adv. Energy Mater.* **2023**, *13*, 2301199.
- [32] S. Chen, J. Zheng, D. Mei, K. S. Han, M. H. Engelhard, W. Zhao, W. Xu, J. Liu, J. G. Zhang, *Adv. Mater.* **2018**, *30*, 1706102.
- [33] X. Ren, S. Chen, H. Lee, D. Mei, M. H. Engelhard, S. D. Burton, W. Zhao, J. Zheng, Q. Li, M. S. Ding, M. Schroeder, J. Alvarado, K. Xu, Y. S. Meng, J. Liu, J.-G. Zhang, W. Xu, *Chem.* **2018**, *4*, 1877.
- [34] X. Zhang, L. Zou, Y. Xu, X. Cao, M. H. Engelhard, B. E. Matthews, L. Zhong, H. Wu, H. Jia, X. Ren, P. Gao, Z. Chen, Y. Qin, C. Kompella, B. W. Arey, J. Li, D. Wang, C. Wang, J. G. Zhang, W. Xu, *Adv. Energy Mater.* **2020**, *10*, 2000368.
- [35] X. Ren, L. Zou, X. Cao, M. H. Engelhard, W. Liu, S. D. Burton, H. Lee, C. Niu, B. E. Matthews, Z. Zhu, C. Wang, B. W. Arey, J. Xiao, J. Liu, J.-G. Zhang, W. Xu, *Joule* **2019**, *3*, 1662.
- [36] X. Zhang, L. Zou, Z. Cui, H. Jia, M. H. Engelhard, B. E. Matthews, X. Cao, Q. Xie, C. Wang, A. Manthiram, J.-G. Zhang, W. Xu, *Mater. Today* **2021**, *44*, 15.
- [37] X. Zhang, H. Jia, Y. Xu, L. Zou, M. H. Engelhard, B. E. Matthews, C. Wang, J.-G. Zhang, W. Xu, *J. Power Sources Adv.* **2020**, *5*, 100024.

- [38] J. Zhang, Q. Zhang, D. Wong, N. Zhang, G. Ren, L. Gu, C. Schulz, L. He, Y. Yu, X. Liu, *Nat. Comm.* **2021**, *12*, 3071.
- [39] Z. Lun, B. Ouyang, Z. Cai, R. J. Clément, D.-H. Kwon, J. Huang, J. K. Papp, M. Balasubramanian, Y. Tian, B. D. McCloskey, H. Ji, H. Kim, D. A. Kitchaev, G. Ceder, *Chem* **2020**, *6*, 153.
- [40] M. J. Crafton, Y. Yue, T. Y. Huang, W. Tong, B. D. McCloskey, *Adv. Energy Mater.* **2020**, *10*, 2001500.
- [41] G. Assat, J.-M. Tarascon, *Nat. Energy* **2018**, *3*, 373.
- [42] X. D. Zhang, J. L. Shi, J. Y. Liang, Y. X. Yin, J. N. Zhang, X. Q. Yu, Y. G. Guo, *Advanced Mater* **2018**, *30*, 1801751.
- [43] J. Ahn, R. Giovine, V. C. Wu, K. P. Koirala, C. Wang, R. J. Clément, G. Chen, *Adv. Energy Mater.* **2023**, *13*, 2300221.
- [44] J. Ahn, Y. Ha, R. Satish, R. Giovine, L. Li, J. Liu, C. Wang, R. J. Clement, R. Kostecki, W. Yang, G. Chen, *Adv. Energy Mater.* **2022**, *12*, 2200426.
- [45] V. S. K Sungjemmenla, C. B. Soni, V. Kumar, Z. W. Seh, *Energy Tech* **2022**, *10*, 2200421.
- [46] Y. Yue, Y. Ha, R. Giovine, R. Clément, W. Yang, W. Tong, *Chem. Mater.* **2022**, *34*, 1524.
- [47] R. J. Clément, D. Kitchaev, J. Lee, C. Gerbrand, *Chem. Mater.* **2018**, *30*, 6945.
- [48] R. Satish, L. Wichmann, M. J. Crafton, R. Giovine, L. Li, J. Ahn, Y. Yue, W. Tong, G. Chen, C. Wang, R. J. Clement, R. Kostecki, *Chem-ElectroChem* **2021**, *8*, 3982.
- [49] W. Yang, T. P. Devereaux, *J. Power Sources* **2018**, *389*, 188.
- [50] Z. Zhuo, K. Dai, R. Qiao, R. Wang, J. Wu, Y. Liu, J. Peng, L. Chen, Y.-d. Chuang, F. Pan, Z.-x. Shen, G. Liu, H. Li, T. P. Devereaux, W. Yang, *Joule* **2021**, *5*, 975.
- [51] G. H. Lee, J. Wu, D. Kim, K. Cho, M. Cho, W. Yang, Y. M. Kang, *Angew. Chem. Int. Ed.* **2020**, *59*, 8681.
- [52] R. Qiao, T. Chin, S. J. Harris, S. Yan, W. Yang, *Current Applied Physics* **2013**, *13*, 544.
- [53] L. Li, B. Ouyang, Z. Lun, H. Huo, D. Chen, Y. Yue, C. Ophus, W. Tong, G. Chen, G. Ceder, C. Wang, *Nat. Commun.* **2023**, *14*, 7448.
- [54] L. Li, J. Ahn, Y. Yue, W. Tong, G. Chen, C. Wang, *Adv. Mater* **2022**, *34*, 2106256.
- [55] L. Li, Z. Lun, D. Chen, Y. Yue, W. Tong, G. Chen, G. Ceder, C. Wang, *Adv. Funct. Mater.* **2021**, *31*, 2101888.
- [56] H. Jia, X. Zhang, Y. Xu, L. Zou, J. M. Kim, P. Gao, M. H. Engelhard, Q. Li, C. Niu, B. E. Matthews, T. L. Lemmon, J. Hu, C. Wang, W. Xu, *ACS Appl. Mater. Interfaces* **2021**, *13*, 44339.
- [57] Y. Xu, H. Jia, P. Gao, D. E. Galvez-Aranda, S. P. Beltran, X. Cao, P. M. L. Le, J. Liu, M. H. Engelhard, S. Li, G. Ren, J. M. Seminario, P. B. Balbuena, J.-G. Zhang, W. Xu, C. Wang, *Nat. Energy* **2023**, *8*, 1345.
- [58] P. Yan, J. Zheng, Z.-K. Tang, A. Devaraj, G. Chen, K. Amine, J.-G. Zhang, L.-M. Liu, C. Wang, *Nat. Nanotechnol.* **2019**, *14*, 602.